LA-UR-17-27560
Approved for public release; distribution is unlimited.

Title: Trade Study for Neutron Transport at Low Earth Orbit: Adding Fidelity to DIORAMA

Author(s): McClanahan, Tucker Caden
Wakeford, Daniel Tyler

Intended for: Report

Issued: 2017-08-22

# Trade Study for Neutron Transport at Low Earth Orbit: Adding Fidelity to DIORAMA

Tucker C. McClanahan, Daniel T. Wakeford

August 17, 2017

## 1 Abstract

The Distributed Infrastructure Offering Real–Time Access to Modeling and Analysis (DIORAMA) software provides performance modeling capabilities of the United States Nuclear Detonation Detection System (USNDS) with a focus on the characterization of Space–Based Nuclear Detonation Detection (SNDD) instrument performance [1]. A case study was done to add the neutron propagation capabilities of DIORAMA to low earth orbit (LEO), and compare the back–calculated incident energy from the time–of–flight (TOF) spectrum with the scored incident energy spectrum. As the scoring altitude lowers, the time increase due to scattering takes up much more of the fraction of total TOF; whereas at geosynchronous earth orbit (GEO), the time increase due to scattering is a negligible fraction of the total TOF [2]. The scattering smears out the TOF enough to make the back–calculation of the initial energy spectrum from the TOF spectrum very convoluted.

## 2 Introduction

This document describes the details of the generation and validation of the neutron propagation data tables for LEO for use in the DIORAMA neutron propagation model. These data tables include the TOF and incident energy spectra for both neutrons and secondary gammas incident on a detector some altitude above the Earth's surface. The DIORAMA neutron propagation model uses these data tables generated by a Monte Carlo code (either the GEANT4 toolkit or Monte Carlo N-Particle (MCNP) code) to propagate the source neutron spectrum (in energy or energy and time) to some altitude of interest above the Earth's surface [3–5]. The LEO data tables are generated using the MCNP6.1 code using the radial atmosphere model described in Wakeford and Hoover's report [3, 4]. The data tables for LEO, mid earth orbit (MEO) and GEO combined only have data up to an altitude of 20,000 km and above 20,000 km, the neutron propagation module applies the $1/r^2$ scaling law and a correction for the free neutron decay lifetime [6]. A case study is also included in this document outlining an investigation into whether the assertion made in previous studies that the TOF is directly related to the incident energy by a kinematic relation is valid at LEO [3, 6]. A description of the pre- and post-processing tools is also included in this document.

# 3 Methods

## 3.1 MCNP Model

### 3.1.1 Geometry

The atmospheric model geometry used in the MCNP calculations contains 204 log-spaced layers of atmosphere from the Earth's surface to 1000 km in altitude [3]. The density and isotopic composition of each atmospheric layer is an average for the thickness of the layer from the NRL MSISE-00 library [3]. Figures 1 and 2 show the X-Y cross section of the atmospheric MCNP model used in all of the calculations for LEO in this document with scales in units of cm. Figure 1 shows the 205 log-based atmospheric layers (the multicolored layers) and the Earth (the green center). Figure 2 shows Figure 1 in context of the full geometry. The outermost structure in Figure 2 is the 1.5E8 $\times$ 1.5E8 $\times$ 1.5E8 m bounding box of the geometry and the white sphere surrounding the atmospheric layers is the GEO sphere with a radius of 4.2164E7 m. The area between the outer radius of the green sphere in Figure 2 and the outer radius of the GEO sphere is where the point detector tallies (discussed in Section 3.1.4 are located. The extent parameters given in the captions of Figures 1 and 2 refers to the MCNP plotting command used to generate the figures and they correspond to the width and height of the geometry viewing area. For Figure 1, the plotting area shown is 2E9 $\times$ 2E9 cm.

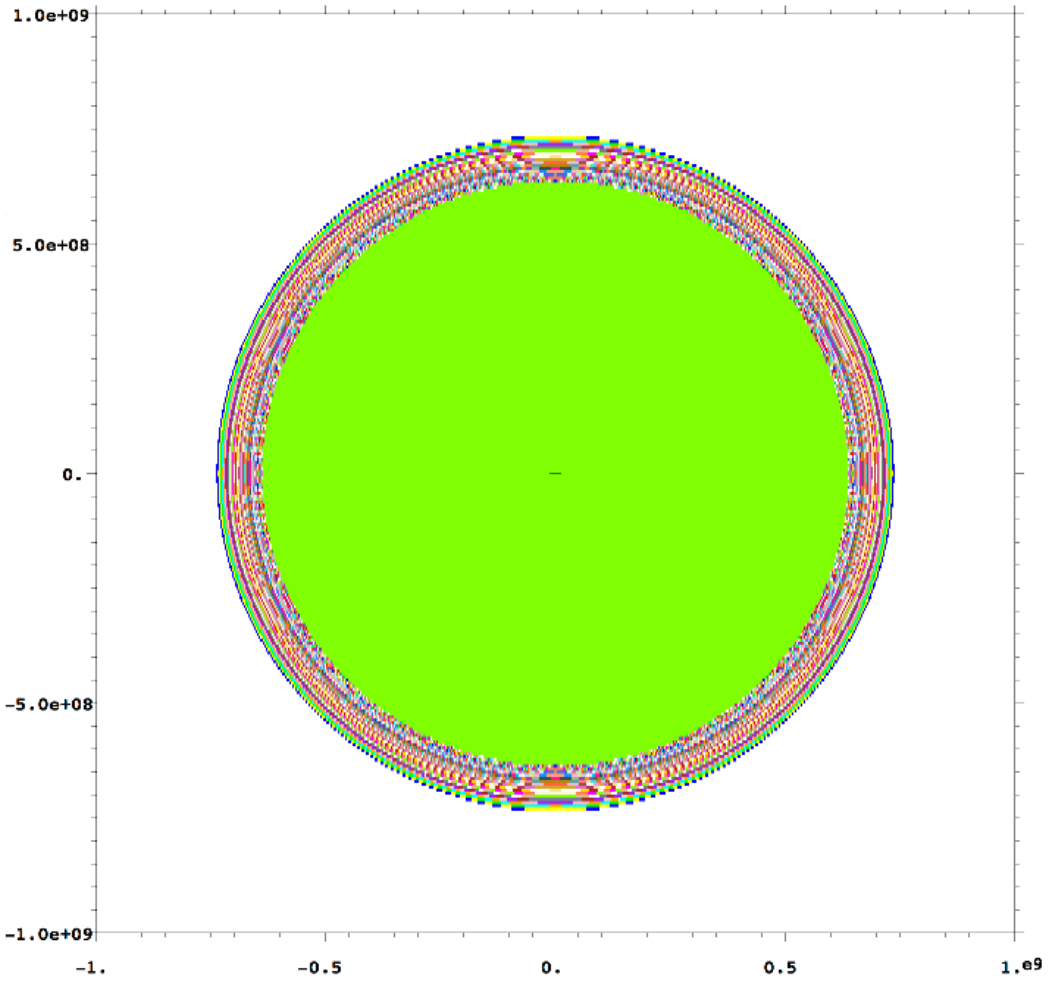


Figure 1: X-Y cross-section of the MCNP atmospheric model with axes in cm, Extent 1E9 1E9

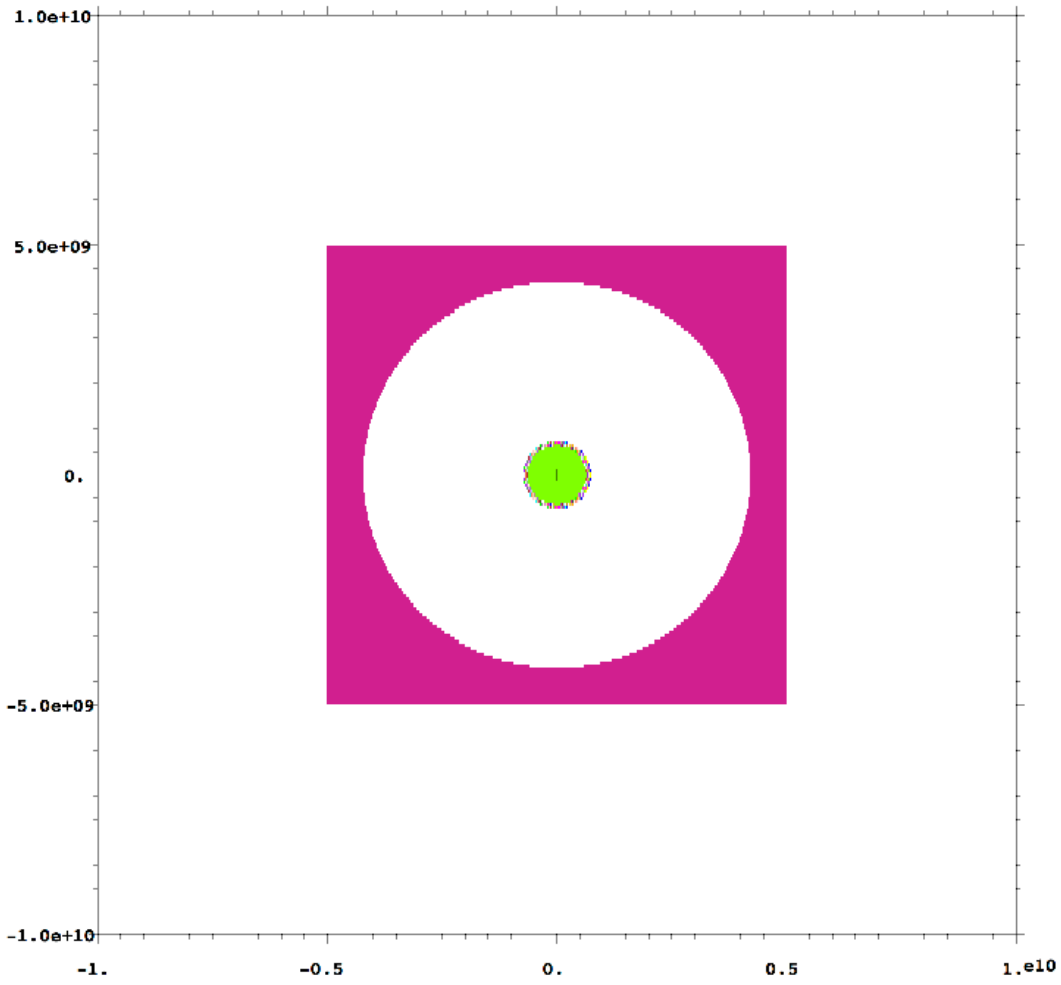


Figure 2: X-Y cross-section of the MCNP atmospheric model with axes in cm, Extent 1E10 1E10

Figure 3 shows the density profile as a function of altitude for the MCNP atmospheric model.

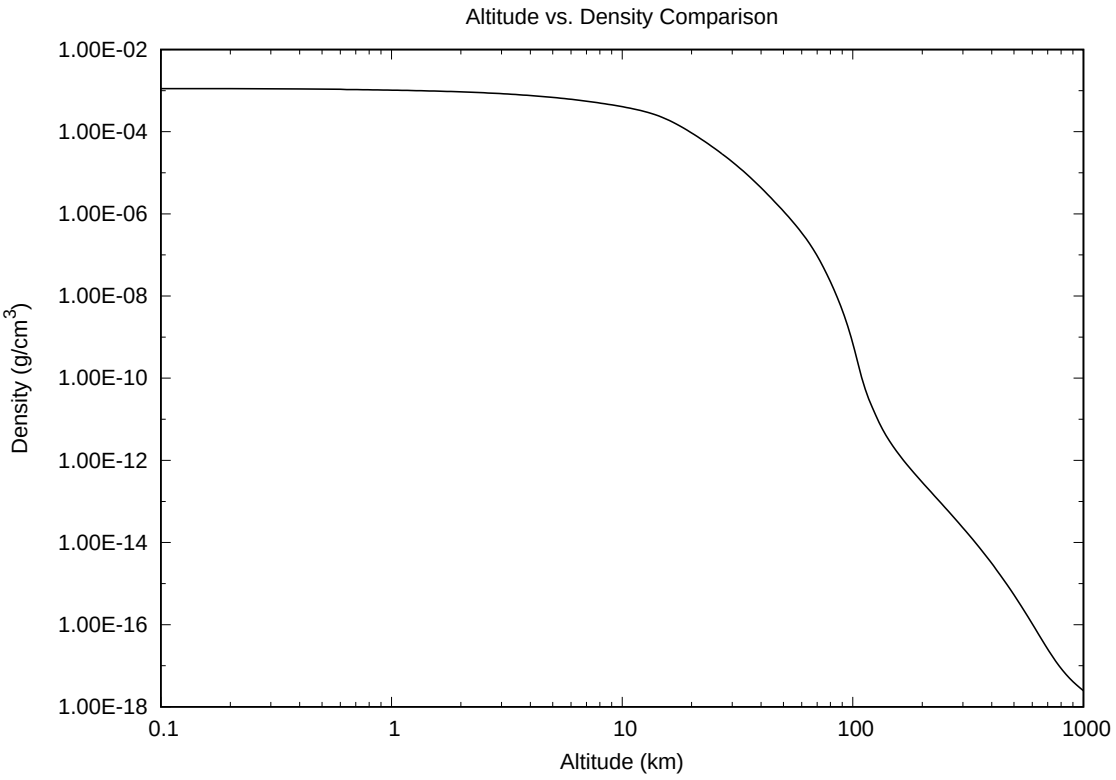


Figure 3: Plot of the altitude versus density for the MCNP atmospheric model

### 3.1.2 Source

The sources used in the creation of the LEO data tables were isotropic monoenergetic point sources located at one of three source altitudes: 20, 70, 400 km. For each source altitude, 126 separate calculations were executed to calculate the TOF for all 126 separate energies of interest. The 126 energies were chosen based on the minimum number of points needed to adequately interpolate the total neutron cross section for the primary atmospheric isotopes:$^{16}$O and $^{14}$N [3]. When all 126 energies were simulated in the same calculation, the TOF data could not be deconvolved from the time-of-arrival (TOA) spectrum incident on the point detectors (discussed in Section 3.1.4) in the calculation due to the effects of scattering at low detection altitudes. The case study described in Section 4.2 elaborates on why the true TOF spectrum for a given neutron source energy cannot be deconvolved from the TOA spectrum incident on the detector.

### 3.1.3 Physics

MCNP6.1 allows the use of both cross section libraries and physics models in the same calculation. The ENDF/B-VII.0 cross section library is the cross section library used in all of the calculations in this document. The neutron upper energy cutoff was set to 100 MeV with analog capture set as the capture mode, and the photon upper energy cutoff was set to 100 MeV with photonuclear production turned on. The cross section library mentioned above was used for energies below 20 MeV.

### 3.1.4 Tallies

In order to gather the flux at various altitudes above Earth's surface, point detector tallies were used at various locations in each calculation. MCNP's point detector tally is what is known as a "next-event estimator" because it is a tally of the flux at a point as if the "next event" in the calculation were a particle traveling with a trajectory directly to the detector point without further collision [7]. Every time there is a particle born or collision event, a contribution is made to the point detector tally. Using MCNP's point detector allows for quicker and more efficient calculations since every history will contribute at least once to all of the point detectors in the calculation.

To produce the LEO data tables, the three source radii (outlined in Section 3.1.2) were paired with five detector radii (300, 500, 700, 900, 1100 km) to form fifteen cases. For each case, ten point detectors were placed at the detector radius for that specific case separated by a polar angle corresponding to a tenth of the horizon polar angle. The polar angle for each detector is defined as the angle between the source radius vector and the detector radius vector. The horizon polar angle is the maximum angle in which the point detector has a direct line-of-sight path with the source without the Earth impinging the path and is shown in Figure 4. Equation 1 shows how the horizon angle ($\theta_H$) is calculated where $R_S$ is the Source Radius, $R_E$ is the Earth's Radius, and $R_D$ is the Detector Radius in Figure 4.

$$\theta_H = \cos^{-1}\left(\frac{R_S^2 + R_D^2 - \left(\sqrt{R_S^2 - R_E^2} + \sqrt{R_D^2 - R_E^2}\right)^2}{2R_S R_D}\right) \tag{1}$$

All of the point detectors in each calculation were positioned at the same azimuthal angle because the neutron flux does not vary with azimuthal angle. The flux at each detector location was tallied in TOA and incident energy.

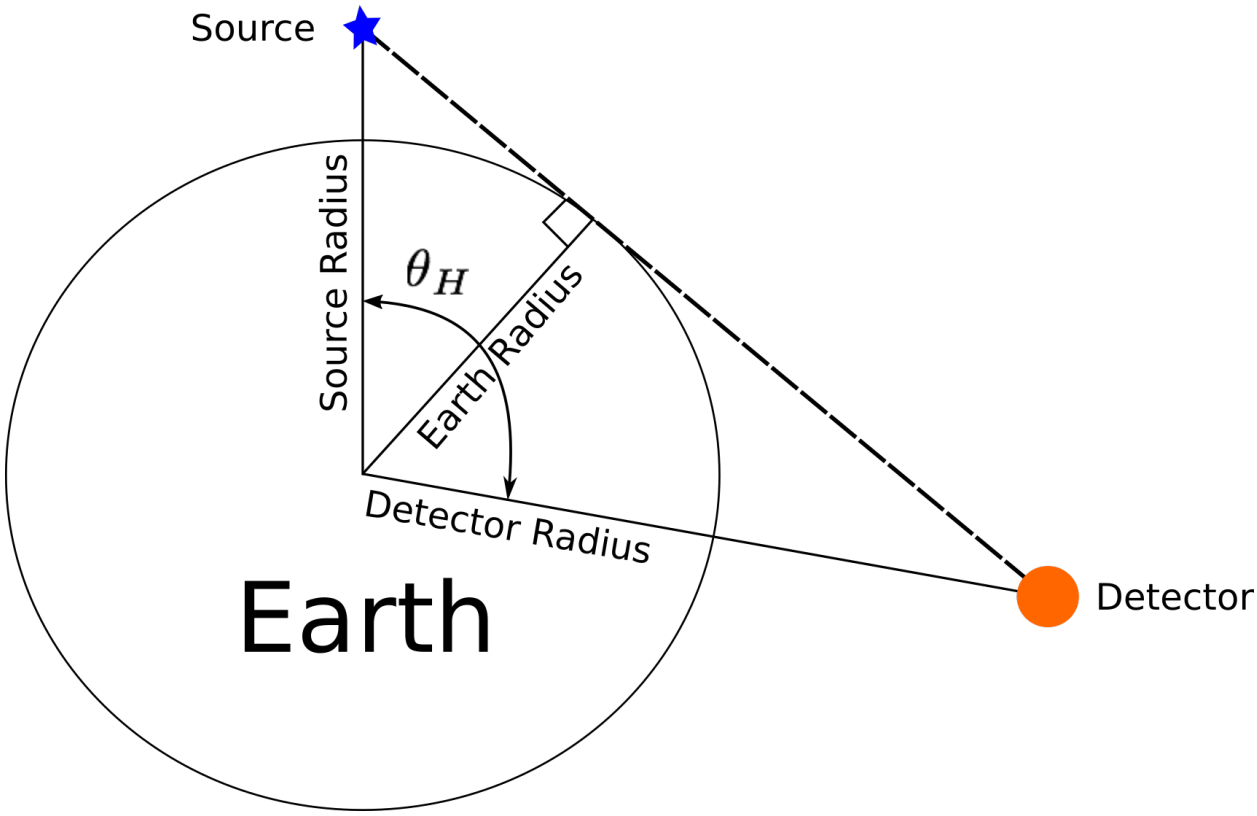


Figure 4: Horizon angle calculation diagram

#### 3.1.5 Variance Reduction

MCNP6.1 includes many variance reduction techniques that can be incorporated with an entry in the input deck. The most important technique used in this simulation was the point detector tally. MCNP includes an implicit absorption feat that is included by default in MCNP where it does not allow any particle to be absorbed, and instead lowers the weight of the particle by the absorption probability [7]. These calculations do not use implicit absorption. Other more elaborate variance reduction techniques using the An Automated Variance Reduction Parameter Generator (ADVANTG) [8] generated weight-windows were tried but they resulted in longer run times with marginal improvements in the variance of the tallies. Energy (1E-9 MeV) and time (200 sec) truncation was used.

### 3.2 Pre- and Post-Processing

Included in the MCNP distribution is a tool called *mcnp_pstudy* that allows for the automatic generation of MCNP input decks based upon the user's input, and can be used for parameter studies, total uncertainty analyses, or repeated calculations with MCNP [9]. *mcnp_pstudy* was used to set up the MCNP calculations used to generate the LEO data tables.

Along with *mcnp_pstudy*, a Python [10] script was used to generate the point detector tallies given the event and detector altitudes. The polar angles used in the placement of the point detector tallies and the time bins for each point detector are a functions of the event and detector altitudes. Every point detector in each calculation has a different time binning depending on the direct TOA of the source neutron.

A Python script was used to process the MCNP mctal file from each calculation to generate separate text files for each tally in the calculation. Also, a series of GNUPLOT [11] and Python scripts generate many of the figures shown in this document. In order to produce the neutron transport matrix (NTM) data files used in DIORAMA, another Python script read in the tally text files from many MCNP calculations and wrote out the respective NTM files.

# 4 Results

## 4.1 NTM Data Files

After fifteen combinations of source and detector altitudes with each combination having 126 separate initial energies propagated to ten point detectors, fifteen NTM files were written corresponding to the combinations. Figure 5 shows an example of the neutron flux data that is written in the NTM files. For every detection angle present in the calculation, the flux data is written to the file in the format shown below where $E_{\#}$ is the incident energy at the center of the bin and $T_{\#}$ is the TOA at the center of the bin: The format shown is written in the file a total of 10 times; once for each detection angle

$$\begin{array}{cccc} \phi(E_1,T_1) & \phi(E_2,T_1) & \cdots & \phi(E_N,T_1) \\ \phi(E_1,T_2) & \phi(E_2,T_2) & \cdots & \phi(E_N,T_2) \\ \vdots & \vdots & \ddots & \vdots \\ \phi(E_1,T_N) & \phi(E_2,T_N) & \cdots & \phi(E_N,T_N) \end{array}$$

The flux data for each detection angle is separated by comments and a "normalization block" of the time-integrated flux values as a function of initial energy with the format as follows where $E_{\#}$ is the incident energy:

$$\begin{array}{cccc} \phi(E_1) & \phi(E_2) & \cdots & \phi(E_N) \end{array}$$

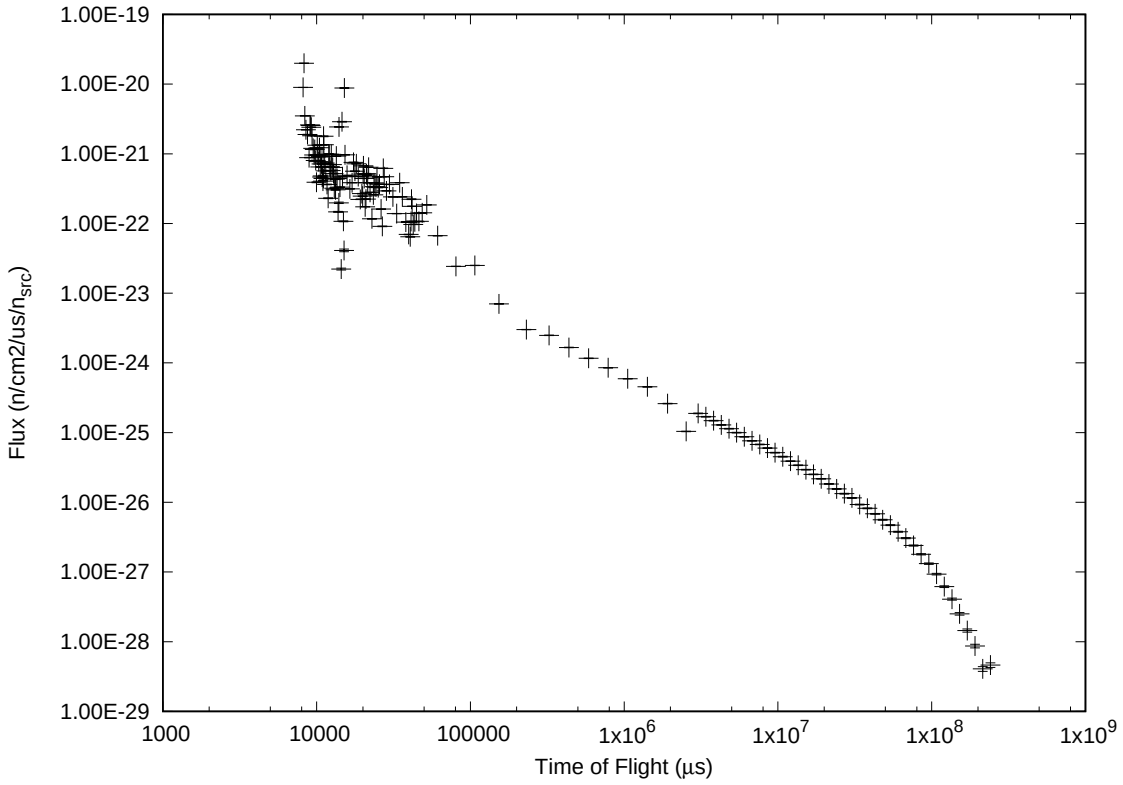


Figure 5: Plot of the TOF spectrum detected at an altitude of 300 km and a polar angle of 2.17 degrees with a source of 10.9 MeV neutrons at an altitude of 20 km.

### 4.2 Case Study

The backcalculation of the incident energy spectrum on a detector from the TOA spectrum on the detector is a straight-forward relativistic kinematic relationship for detectors located at GEO because the scattering time for a given source neutron is a negligible fraction of the total time that it takes the neutron to reach the detector. Therefore, the TOA is equal to the TOF of the neutron of a given source energy at GEO. However, it has been proposed that this relativistic kinematic relationship breaks down at LEO due to the scattering time for a given source neutron being a significant fraction of the total time it takes for the neutron to reach the detector [2]. The case study described in this section validates the assumption that the relativistic kinematic relationship breaks down at LEO. For the MCNP calculations in the case study, all 126 energies (from 100 eV to 20 MeV) were simulated with an isotropic emission in the same calculation, and the model geometry and physics are the same as what is described earlier in this document.

Figure 6 shows the scored energy spectrum (Scored) and the calculated energy spectrum (Calculated) from the scored time of arrival (TOA) at the same detector point.

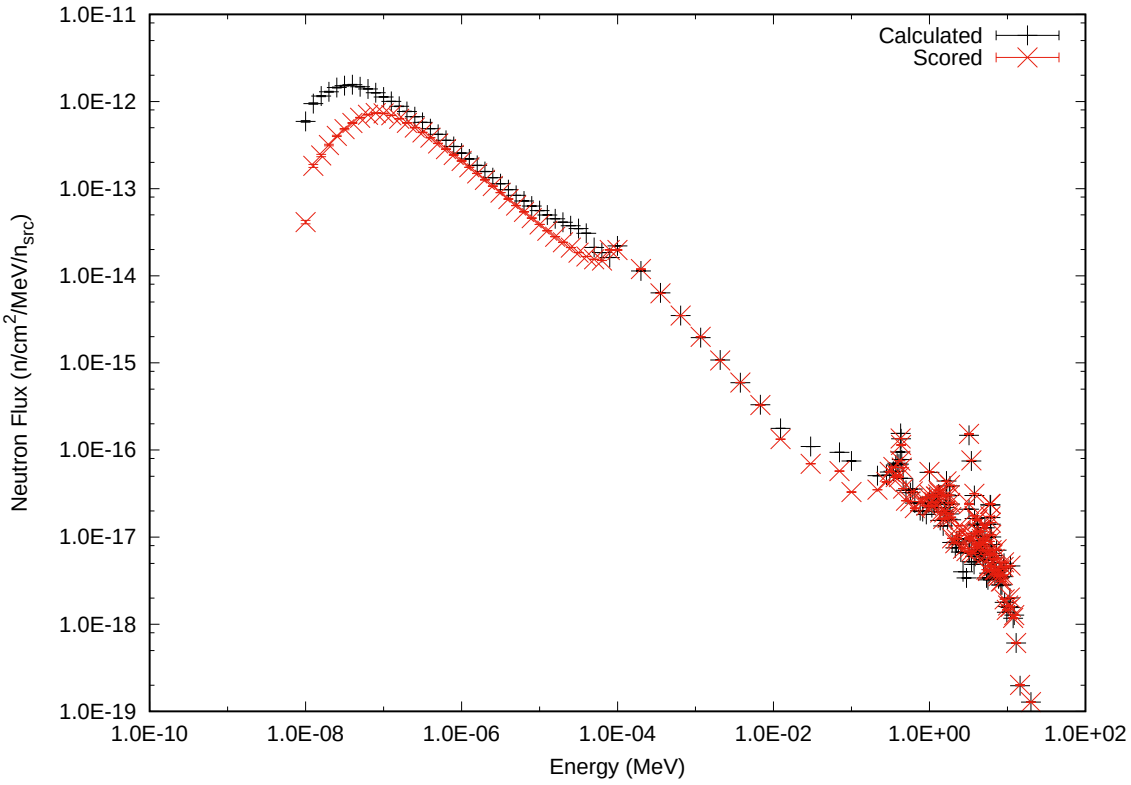


Figure 6: Simulated vs. Calculated energy spectrum for an event at 100 km with a detector at 400 km at 0 degrees

The descrepancies between the two spectra in Figure 6 are present in both the lower and upper energy regions. The descrepancies stem from neutrons traveling most of the distance to the detector and then being scattered close to the detector and thus showing up at in a time bin that is much quicker than the time bin associated with a neutron of the same incident energy. Figure 7 shows some possible paths a neutron can take to the detector.

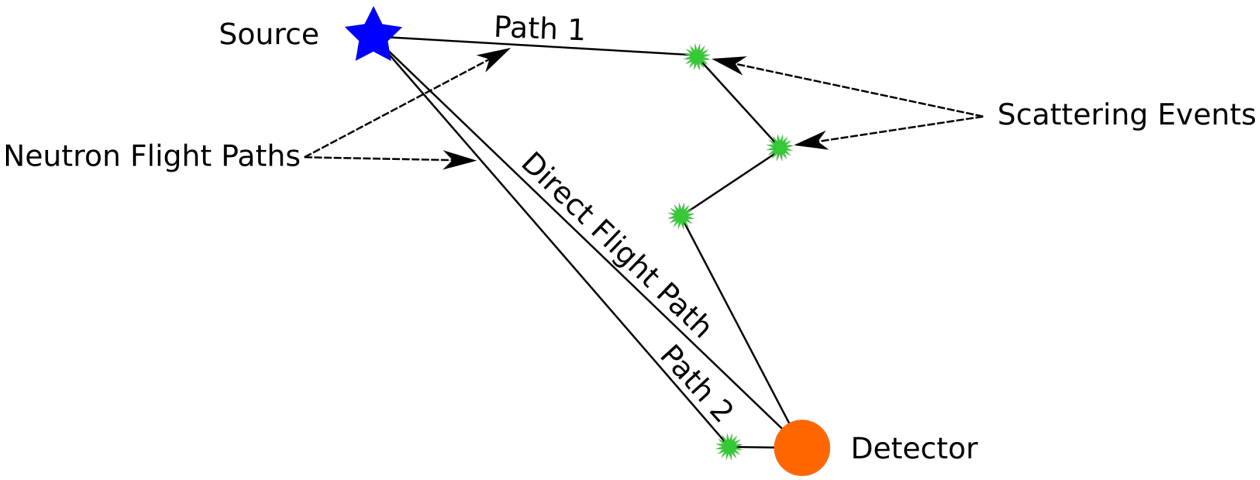


Figure 7: Diagram of the various possible neutron paths from source to detector

The direct, unscattered flight path is shown as the middle flight path from source to detector. Path 1 in Figure 7 shows the path of a neutron that has been scattered several times and thus will show up in a lower incident energy bin and slower time bins. Path 2 in Figure 7 shows a much different path where the neutron has traveled most of the way to the detector as one energy and then right before it gets to the detector, it undergoes a scattering event and thus changes the energy of the neutron. Since the neutron in path 2 in Figure 7 scattered so close to the detector, the TOA is only slightly increased by the scattering event and thus shows up in a time bin that is more indicative of a neutron with the original source energy of the neutron on path 2. However, the neutron hits the detector at a much different energy due to the collision so close to the detector. By using the relativistic kinematic relationship to convert TOA to incident energy, the assumption is made that the incident TOA directly corresponds to the initial source energy of the neutron. That assumption is valid at GEO where the additional time it takes the neutron to scatter in the atmosphere is a negligible fraction of the total time it takes the neutron to travel to the detector. However, at LEO, this additional time it takes the neutron to scatter is a large portion of the total TOF of that neutron. In order to get the true TOF for a neutron of a given source energy from a detector at LEO, the source energy of the neutron must be known in order to deconvolve the TOF spectrum for that neutron of a given source energy from the TOA spectrum (which is a convolution of the TOF spectrum for all neutron source energies). Figures 8 and 9 show the flux as a function of energy scored and TOA for an event height at 100 km with a detector radius at 400 km at a polar angle of approximately 12 degrees. The line going through Figures 8 and 9 shows the relationship between TOA and incident energy in a void where TOF is equal to the TOA for a neutron of a given source energy. However, at the lower altitude, the scattering dominates. Neutrons that arrive sooner than the time it would take to travel unscattered for a given energy are to the left of the line going through the figures. This effect is not seen at GEO. Figures 10 and 11 demonstrate that the fraction of time it takes for the neutron to scatter over the direct TOF is so small that it cannot be distinguished from the direct TOF. Figures 10 and 11 show that the bottom corner of every bin follows the line. Note that in these plots the data trend appears to diverge from the straight line but that this is due to nonlinear bin sizes in the plot.

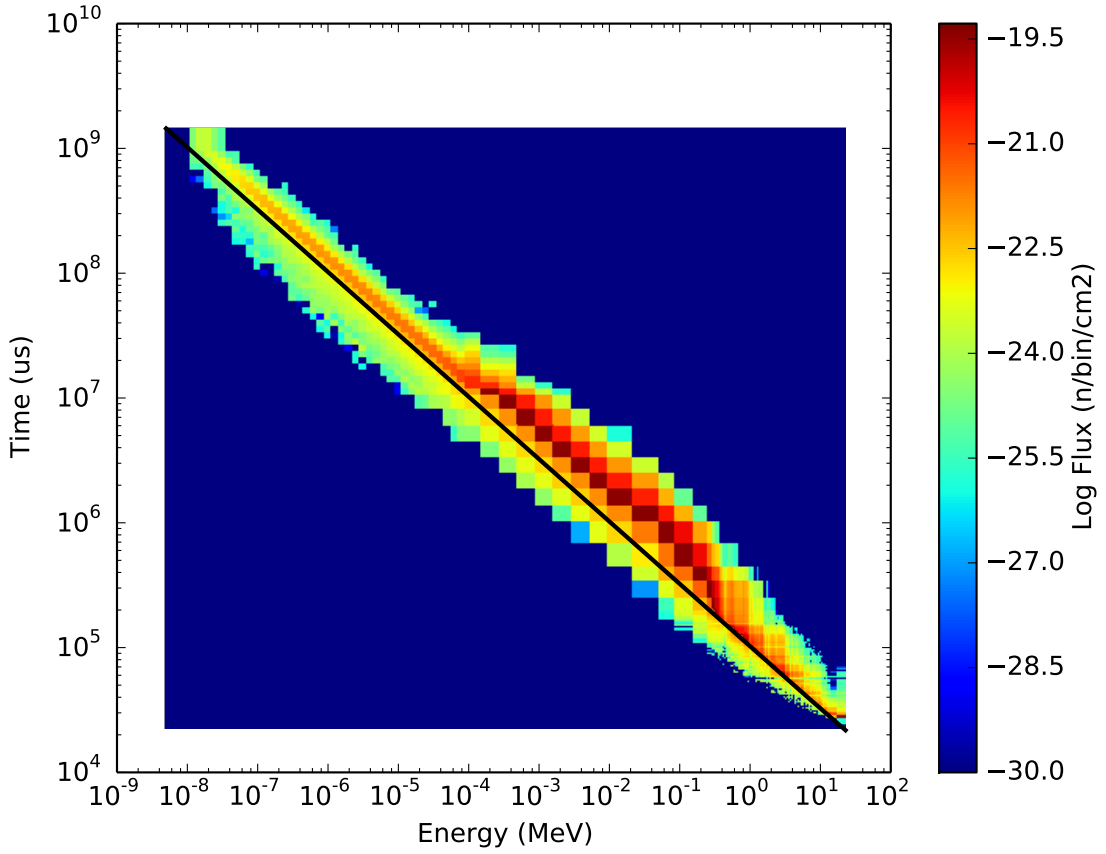


Figure 8: Flux values for given time of arrivals (TOA) and scored energy for an event height of 100 km, detector radius of 400 km at an angle of 12 degrees

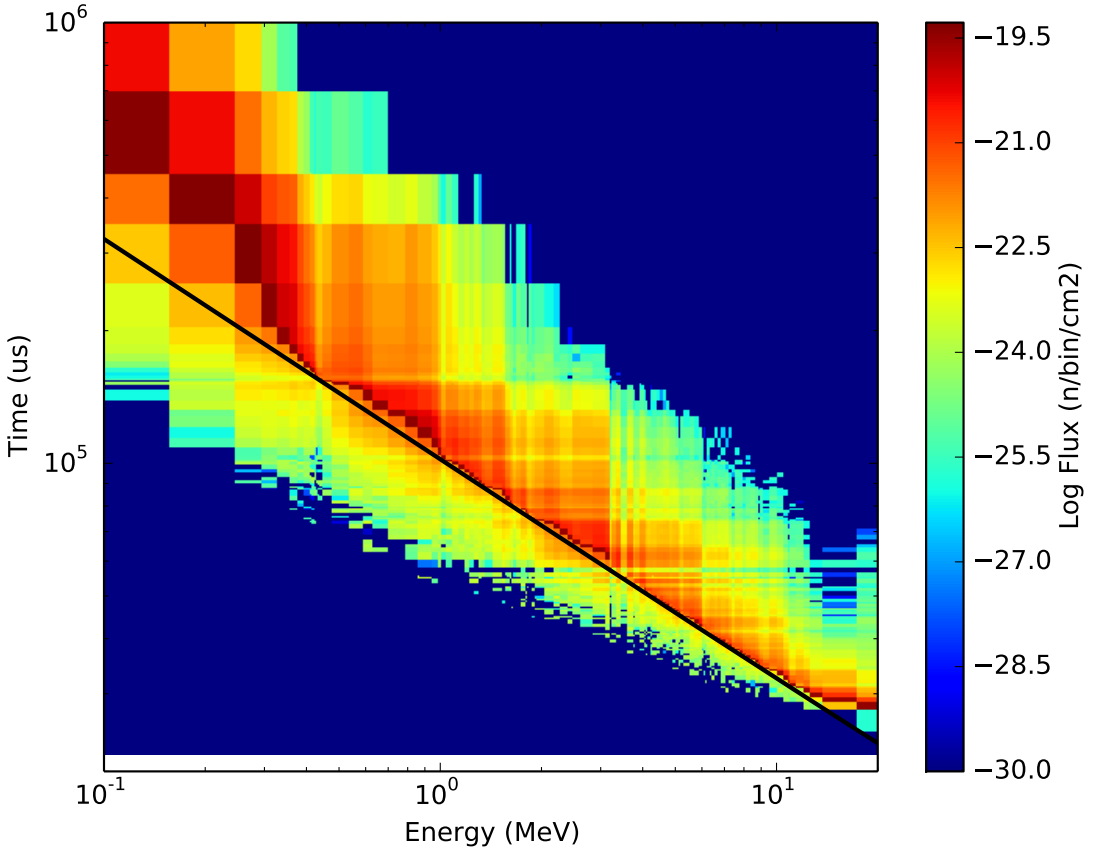


Figure 9: Flux values for given time of arrivals (TOA) and scored energy for an event height of 100 km, detector radius of 400 km at an angle of 12 degrees focused on 0.1 to 20 MeV

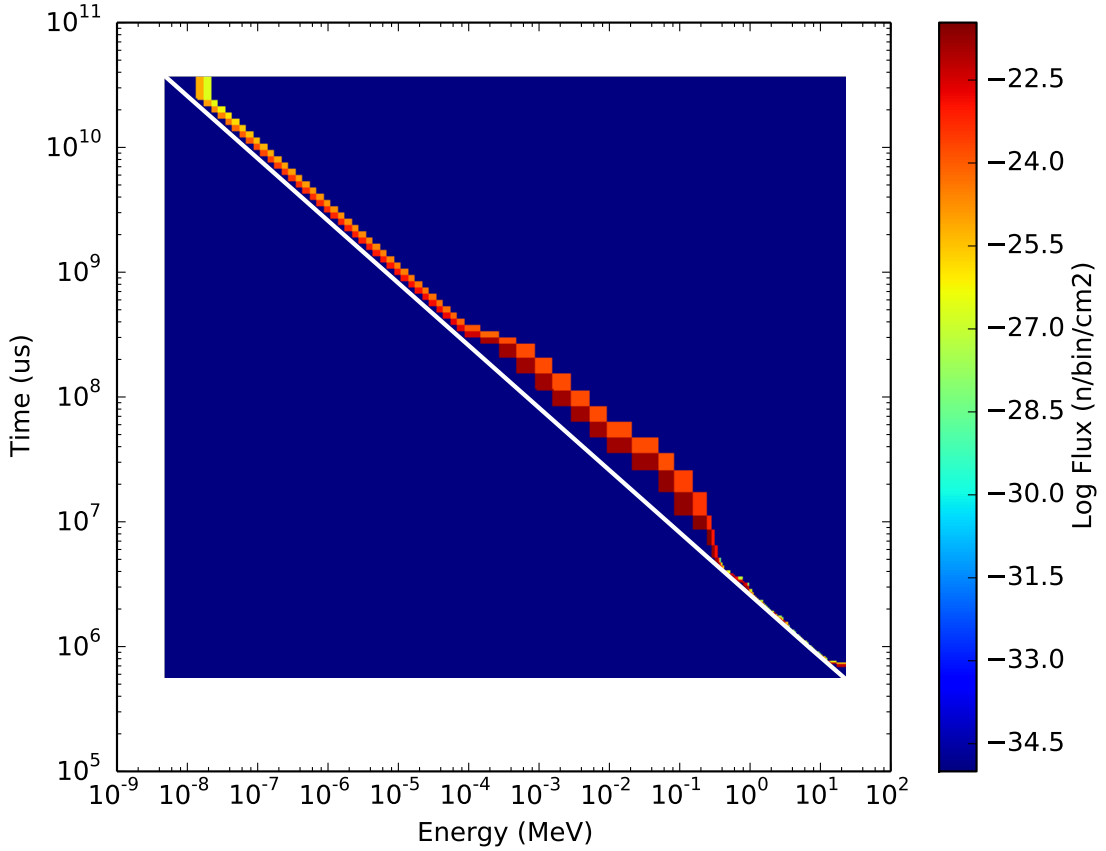


Figure 10: Flux values for given time of arrivals (TOA) and scored energy for an event height of 100 km, detector radius of GEO km at an angle of 0 degrees

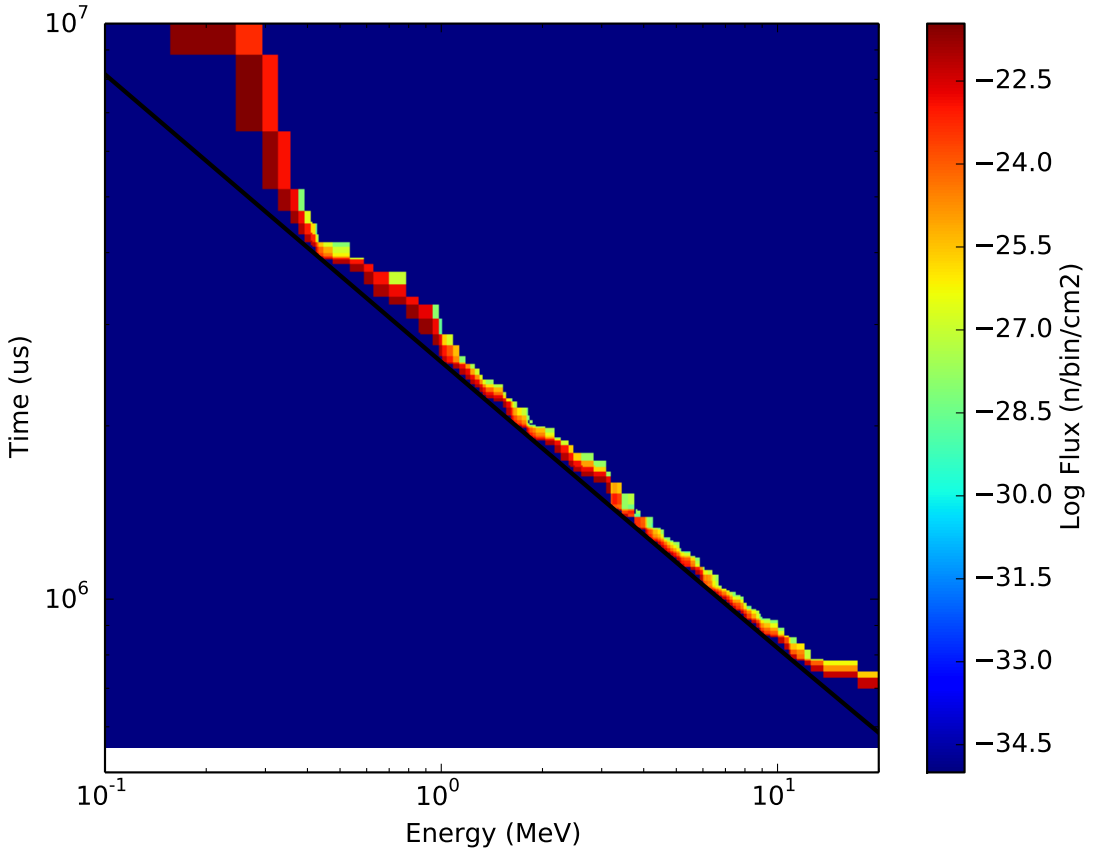


Figure 11: Flux values for given time of arrivals (TOA) and scored energy for an event height of 100 km, detector radius of GEO km at an angle of 0 degrees focused on 0.1 to 20 MeV

The metric used to compared the scored energy spectrum and the calculated energy spectrum from TOA is shown Equation 2.

$$\text{FOM} = \sum \frac{\text{Scored} - \text{Calculated}}{\text{Scored}} \tag{2}$$

The Scored and Calculated values are shown in Figure 6. The FOM shown in Equation 2 proved to be an effective way to simply demonstrate the magnitude of the difference between the two spectra. Equation 2 described above which only accounts for the center of the bin. The goal of finding a metric of agreement was to find a region of phase space that the TOA backcalculation is valid. A low FOM corresponds to better agreement.

A couple of examples of the resulting FOM values are shown in Figures 12 and 13. Figures 12 and 13 show that for a given detector altitude, the FOM worsens with the increase of polar angle. The differences arise from the increased distance from source to detector and the resulting higher scattering probability. The FOM worsens with distance from GEO. The rise in FOM is a result of the fraction of scattering distance to total TOF getting larger as the total distance from source to

detector decreases. Figures 12 and 13 show that the more that the detector altitude approaches GEO, the more valid the backcalculation becomes.

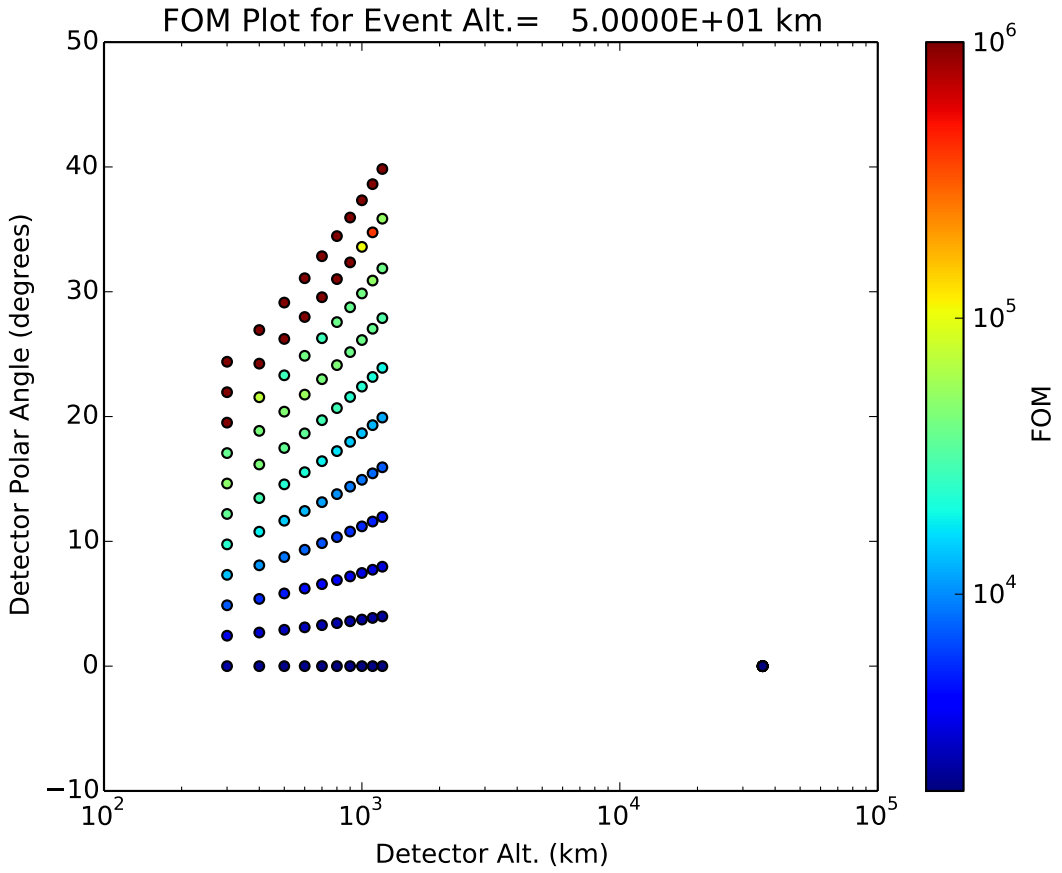


Figure 12: FOM plot for an event altitude of 50 km where the FOM is the sum of the fractional differences

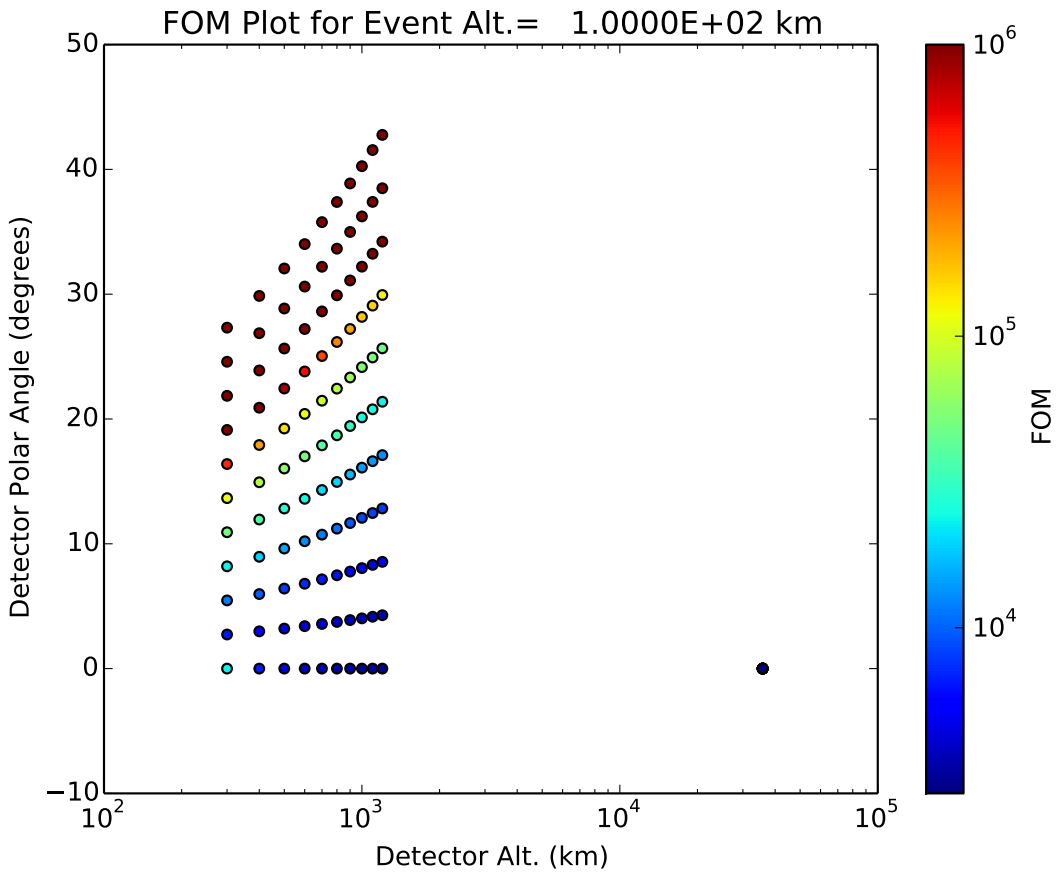


Figure 13: FOM plot for an event altitude of 100 km where the FOM is the sum of the fractional differences

Figures 14 and 15 show the FOM values for each detector polar angle versus event altitude. For both detection altitudes, as the detector polar angle increases, the FOM increases. The increase is due to the enhanced scattering effects produced by traveling through more material with the increased detector polar angle. Due to the enhanced scattering effects, the relationship worsens between the scored and TOA-calculated incident energy spectra.

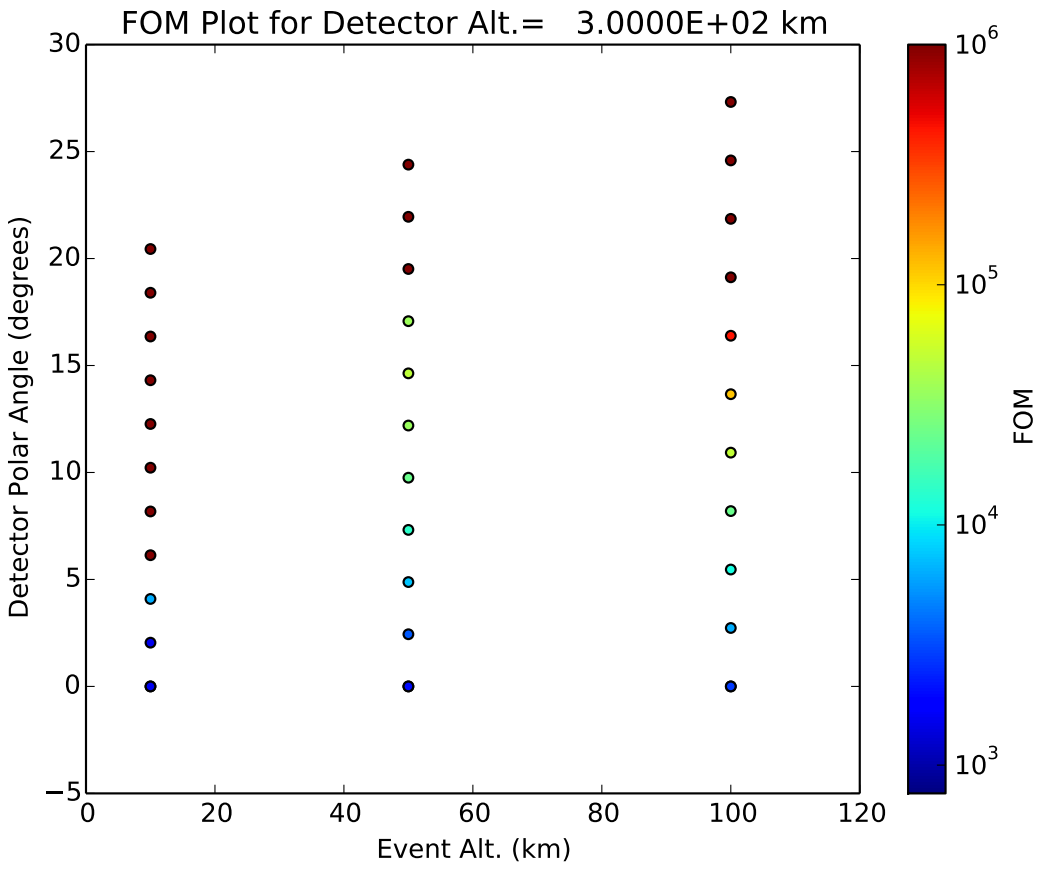


Figure 14: FOM plot for a detection of 300 km where the FOM is the sum of the fractional differences

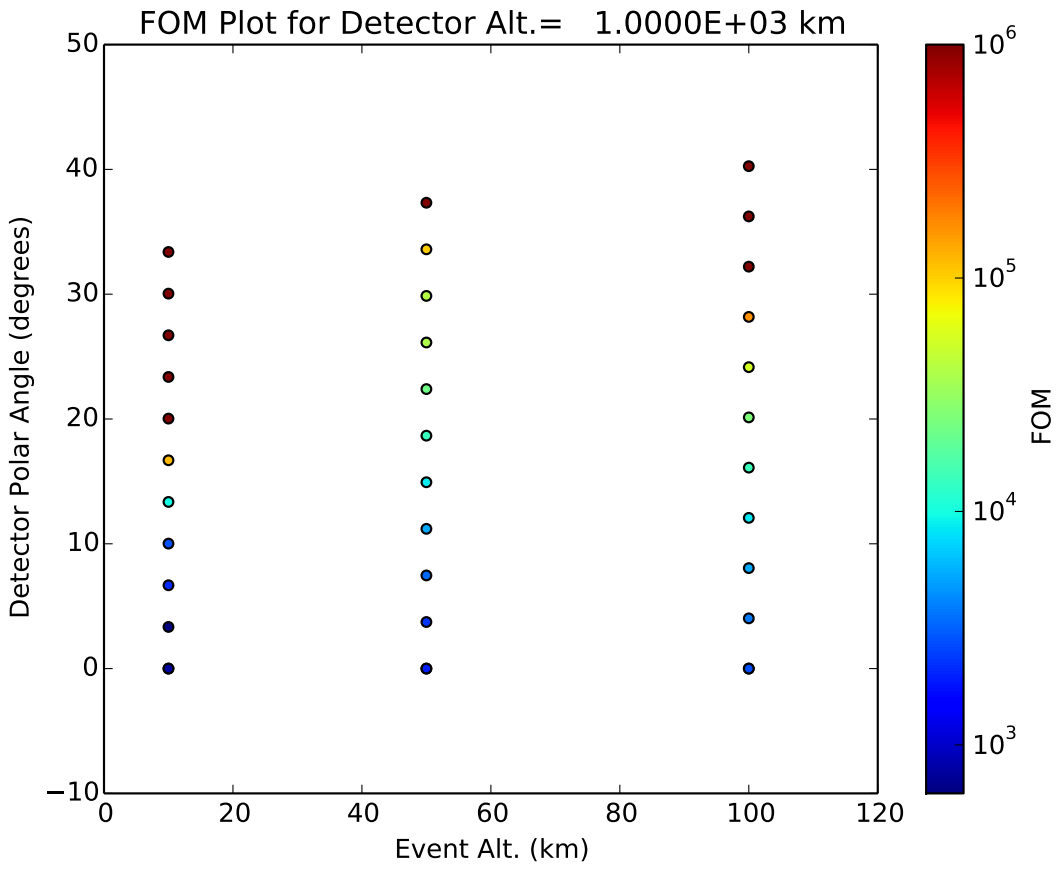


Figure 15: FOM plot for a detection of 300 km where the FOM is the sum of the fractional differences

## 5 Conclusions

The LEO neutron flux data for the neutron propagation module at three event altitudes, five detector altitudes and ten polar angles for each event and detector altitude combination was produced by an MCNP model consisting of 204 atmospheric layers. Validation steps were taken to investigate whether the assumption that the TOA incident upon the detector could be used to back–calculate the incident energy spectrum on the detector at LEO. This study finds that the differences between actual and TOA–calculated energy spectra at LEO are greater than at GEO.

## References


[1] B. Norman, "DIORAMA Overview," Tech. Rep. LA-UR-13-28282, LANL, 2013. Sponsor: DOE/LANL.

[2] R. C. Byrd and B. D. Heerema, "Atmospheric Transport of Neutrons and Gamma Rays from Near-Horizon Nuclear Detonations," Tech. Rep. LA-13099-MS, LANL.

[3] D. T. Wakeford and A. S. Hoover, "Neutron Propagation in DIORAMA v1.4," Tech. Rep. LA-CP-17-20196, LANL, Apr. 2017.

[4] J. T. Goorley, M. L. Fensin, G. W. McKinney, M. R. James, R. A. Forster, D. B. Pelowitz, T. E. Booth, and J. S. Hendricks, "MCNP6 User's Manual," Tech. Rep. LA-CP-13-00634, LANL, May 2013.

[5] S. Agostinelli, J. Allison, K. Amako, J. Apostolakis, H. Araujo, P. Arce, M. Asai, D. Axen, S. Banerjee, G. Barrand, F. Behner, L. Bellagamba, J. Boudreau, L. Broglia, A. Brunengo, H. Burkhardt, S. Chauvie, J. Chuma, R. Chytracek, G. Cooperman, G. Cosmo, P. Degtyarenko, A. Dell'Acqua, G. Depaola, D. Dietrich, R. Enami, A. Feliciello, C. Ferguson, H. Fesefeldt, G. Folger, F. Foppiano, A. Forti, S. Garelli, S. Giani, R. Giannitrapani, D. Gibin, J. G. Cadenas, I. Gonzlez, G. G. Abril, G. Greeniaus, W. Greiner, V. Grichine, A. Grossheim, S. Guatelli, P. Gumplinger, R. Hamatsu, K. Hashimoto, H. Hasui, A. Heikkinen, A. Howard, V. Ivanchenko, A. Johnson, F. Jones, J. Kallenbach, N. Kanaya, M. Kawabata, Y. Kawabata, M. Kawaguti, S. Kelner, P. Kent, A. Kimura, T. Kodama, R. Kokoulin, M. Kossov, H. Kurashige, E. Lamanna, T. Lampn, V. Lara, V. Lefebure, F. Lei, M. Liendl, W. Lockman, F. Longo, S. Magni, M. Maire, E. Medernach, K. Minamimoto, P. M. de Freitas, Y. Morita, K. Murakami, M. Nagamatu, R. Nartallo, P. Nieminen, T. Nishimura, K. Ohtsubo, M. Okamura, S. O'Neale, Y. Oohata, K. Paech, J. Perl, A. Pfeiffer, M. Pia, F. Ranjard, A. Rybin, S. Sadilov, E. D. Salvo, G. Santin, T. Sasaki, N. Savvas, Y. Sawada, S. Scherer, S. Sei, V. Sirotenko, D. Smith, N. Starkov, H. Stoecker, J. Sulkimo, M. Takahata, S. Tanaka, E. Tcherniaev, E. S. Tehrani, M. Tropeano, P. Truscott, H. Uno, L. Urban, P. Urban, M. Verderi, A. Walkden, W. Wander, H. Weber, J. Wellisch, T. Wenaus, D. Williams, D. Wright, T. Yamada, H. Yoshida, and D. Zschiesche, "Geant4 - a simulation toolkit," *Nuclear Instruments and Methods in Physics Research Section A: Accelerators, Spectrometers, Detectors and Associated Equipment*, vol. 506, no. 3, pp. 250 – 303, 2003.

[6] A. S. Hoover, "DIORAMA Neutron Propagation," Tech. Rep. LA-UR-16-21802, LANL, Mar. 2016.

[7] X-5 Monte Carlo Team, "Mcnp - a general monte carlo n-particle transport code, version 5," Tech. Rep. LA-UR-03-1987, LANL, Apr. 2003.

[8] S. W. Mosher, A. M. Bevill, S. R. Johnson, A. M. Ibrahim, C. R. Daily, T. M. Evans, J. C. Wagner, J. O. Johnson, and R. E. Grove, "ADVANTG - An Automated Variance Reduction Parameter Generator," Tech. Rep. ORNL/TM-2013/416, ORNL, Nov. 2013.

[9] F. B. Brown, J. E. Sweezy, and R. Hayes, "Monte Carlo Parameter Studies and Uncertainty Analyses with MCNP5," Tech. Rep. LA-UR-04-0499, LANL, Apr. 2004.

[10] G. Rossum, "Python Reference Manual," tech. rep., Amsterdam, The Netherlands, The Netherlands, 1995.

[11] T. Williams and C. Kelley, "Gnuplot 5.0: An Interactive Plotting Program," April 2015.

[12] W. H. Press, S. A. Teukolsky, W. T. Vetterling, and B. P. Flannery, *Numerical Recipes in FORTRAN; The Art of Scientific Computing*. New York, NY, USA: Cambridge University Press, 2nd ed., 1993.